Nonlinear Semi-Analytical Model for Axial Flux Permanent-Magnet Machine

Guo, Baocheng; Du, Yunlu; Djelloul KHEDDA, Zakarya; Peng, Fei; Dong, Jianning; Huang, Yunkai; Frederic, Dubas; Boughrara, Kamel

DOI
10.1109/TIE.2022.3159952

Publication date
2022

Document Version
Final published version

Published in
IEEE Transactions on Industrial Electronics

Nonlinear Semianalytical Model for Axial Flux Permanent-Magnet Machine

Baocheng Guo, *Member, IEEE*, Yunlu Du, Zakarya Djelloul-Khedda, Fei Peng, *Member, IEEE*, Jianning Dong, *Member, IEEE*, Yunkai Huang, Frédéric Dubas, and Kamel Boughrara

***Abstract*—In this article, we propose a novel nonlinear semianalytical model (AM) for the magnetic field calculation of electric machines. The nonlinear properties and local saturation effect of the iron part are taken into consideration in Cartesian coordinates, which is the main contribution of the proposed model. Thus, high accuracy of electromagnetic field results can be obtained with the low computational time cost. The model is developed based on the harmonic modeling technique by solving Maxwell's equations. The detailed theoretical derivations, which use the complex Fourier series and the Cauchy product, are presented. To verify the proposed model, an axial flux permanent-magnet (PM) machine is selected to be investigated. Both finite-element model and experimental results agree well with that of the proposed model. Moreover, the nonlinear AM has potential application for other types of PM electrical motor in Cartesian coordinates, such as flat PM linear machines.**

***Index Terms*—Axial flux permanent-magnet machine (AFPMM), Cartesian coordinates, harmonic model, saturation effect.**

I. Introduction

COMPARED with radial flux permanent-magnet (PM) machines, axial flux permanent-magnet machines (AFPMMs) have attracted lots of engineering researchers' attention due to their higher power density, torque density, and efficiency [1]–[3]. Thanks to these features, they have been successfully applied to industrial fields, for instance, electric vehicle traction motor, cooling fan, aircraft drive, and submarine drive [4]. It is worthy to point out that the magnetic structure of the AFPMM has a strong three-dimensional (3-D) effect, viz., the magnetic dimension along the radial direction is different at each radius, which brings challenges for the motor design.

In the field of machine modeling, numerical simulation, viz., finite-element model (FEM), is applied widely in academia and industry due to its excellent accuracy. As for AFPMMs, 3-D FEM can obtain the magnetic flux density precisely, and the computational time for 3-D FEM is long, which is often measured by hours or days. Instead of obtaining data from 3-D FEM, designers can use the quasi 3-D–2-D method to reduce the computational time. However, this method still takes three or five times longer than the traditional radial flux PM machines [5]. Hence, FEM is not a good choice for the initial design of AFPMM.

Alternative approaches are analytical or hybrid methods [6]. The magnetic equivalent circuit or the reluctance/permeance network is commonly used [7]–[9]. This type of modeling has good tradeoff between simplicity and accuracy. However, as for some magnetic qualities, such as cogging torque waveforms and force waveforms, it is highly dependent on the number of nodes and solution strategy [10].

The analytical method uses mathematical expression and solves Maxwell's equations to achieve the magnetic field in the air gap. In such a way, the computational time is less. Until now, several analytical models (AMs) have been developed and proposed, such as Schwarz–Christoffel (SC) mapping [11] and subdomain model (SDM) [12]. The relative permanence in the air gap could be obtained by SC mapping, which can reflect the slotting effect in the magnetic field distribution [13], [14]. The SDM uses the separation of variables method to obtain the general expression of each domain [15], [16]. However, most of the AMs are developed based on one main assumption, which is that iron materials have infinite permeance; this means that the saturation effect in a ferromagnetic material is ignored. Hence, the calculation accuracy of electromagnetic performance is reduced under heavy load working conditions.

To solve the aforementioned problems, two calculation approaches are brought. One is the exact SDM proposed by Dubas and Boughrara [17], which introduces the global magnetic saturation of the iron core in the analytical solution by using the

Manuscript received October 4, 2021; revised January 2, 2022 and February 15, 2022; accepted March 3, 2022. Date of publication March 22, 2022; date of current version May 2, 2022. This work was supported in part by the National Natural Science Foundation of China under Grant 51777034 and Grant 51907027. *(Corresponding author: Yunlu Du.)*

Baocheng Guo is with the School of Electrical and Automation Engineering, Nanjing Normal University, Nanjing 210023, China (e-mail: bc.guo@njnu.edu.cn).

Yunlu Du, Fei Peng, and Yunkai Huang are with the School of Electrical Engineering, Southeast University, Nanjing 210096, China (e-mail: duyl@seu.edu.cn; pengfei@seu.edu.cn; huangyk@seu.edu.cn).

Zakarya Djelloul-Khedda is with the LESI Laboratory, Djilali Bounaama University of Khemis Miliana, Khemis Miliana 44225, Algeria (e-mail: djelloulkhedda.zakarya@chlef.sadeg.dz).

Jianning Dong is with the Department of Electrical Sustainable Energy, Delft University of Technology, 2628 DC Delft, The Netherlands (e-mail: j.dong-4@tudelft.nl).

Frédéric Dubas is with the département ENERGIE, FEMTO-ST, CNRS, Univ. Bourgogne Franche-Comté, F90000 Belfort, France (e-mail: frederic.dubas@univ-fcomte.fr).

Kamel Boughrara is with the Laboratoire de Recherche en Electrotechnique (LRE), Ecole Nationale Polytechnique, Algiers 16200, Algeria (e-mail: kamel.boughrara@g.enp.edu.dz).

Color versions of one or more figures in this article are available at https://doi.org/10.1109/TIE.2022.3159952.

Digital Object Identifier 10.1109/TIE.2022.3159952

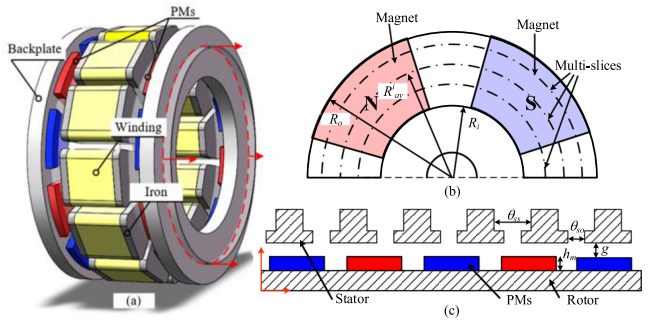

Fig. 1. Prototype model of AFPMM. (a) 3D model. (b) Multi-slices model. (c) 2D calculation section.

principle of superposition in both directions. These techniques have been extended and applied to rotary and linear electrical machines [18], [19]. The local magnetic saturation effect with the *B(H)* curve has also been introduced in the analytical solution [20] by dividing the stator and/or rotor regions with(out) electrical conductivities into elementary subdomains. Another approach is the harmonic modeling (HM) technique developed by Sprangers *et al.* [21], [22]. Different from exact or elementary SDM, the HM technique considers the permeance of the iron part and embeds it into the complex general solutions. Djelloul-Khedda *et al.* [23] consider the local magnetic saturation in the iron parts and calculate the electromagnetic performance of the switched reluctance machine. Further work is carried out by Zhao *et al.* [24] in the magnetic performance prediction and optimize the magnetic gear. From the literature survey, we can learn that the HM technique can consider the nonlinear properties of materials. However, all previous studies analyzed the radial flux motors in polar coordinates, not in Cartesian coordinates. As for the AFPMMs and PM linear machines, which are modeled in Cartesian coordinates, there are no solutions yet.

In this article, the nonlinear semi-AM based on the HM approach, which is modeled in Cartesian coordinates, is developed and presented. The proposed model divides the iron into several parts, and the nonlinear and local magnetic saturation effect of stator iron is considered by iterative strategy. The quality of the results obtained from the proposed HM technique is compared with that of the FEM, and it is shown that the proposed model has high accuracy as the FEM and much lower computational time than the FEM. Moreover, the proposed model has significant value for the design and the optimization of other types of electric motors modeled in Cartesian coordinates.

The rest of this article is organized as follows. Section II provides the geometry parameters and magnetic calculation simplification of the AFPMM. The detailed derivation for the HM approach in Cartesian coordinates is presented in Sections III and IV. In Section V, the results of the proposed model are compared with the FEM. Meanwhile, the prototype is tested to verify the model further. Finally, Section VI concludes this article.

II. Studied AFPMM

Fig. 1(a) shows the 3-D model of the studied AFPMM. Normally, to reduce the computational time, the quasi-3-D method is used to convert a 3-D model to a 2-D model. The annular calculation section along the axial circumference of the AFPMM is made for dimensionality reduction. Then, expanding the annular calculation section, the 3-D AFPMM is equivalent to a combination of n_s 2-D PM linear motors without the end effect. The schematic of dimensionality reduction is shown in Fig. 1(b) and (c).

TABLE I
Main Dimensions and Parameters of the Studied Machine

AFPMM Quantity	Symbol	Value
Rated power	P	1 hp
Rated speed	n_{sp}	3,600 rpm
Rated current	I	2.7A
Number of pole pairs/slots	p/Q_s	10/12
Outer/inner radius of AFPMM	R_o^a/R_i^a	105/67.8 mm
Length of the air gap	g	2.2 mm
Remanence of magnet	Br	1.05 T
Magnet Height	h_{pm}	1.7mm
Active Length	L_{stk}	18.95mm

The average radius R^i_{av} of the ith layer is given by

$$R^i_{\text{av}} = R_i + \frac{R_o - R_i}{n_s}(i - 0.5), \quad i = 1, 2, \ldots, n_s \tag{1}$$

$$t_{cp} = \frac{R_o - R_i}{n_s} \tag{2}$$

where n_s is the number of the slices, and t_{cp} is the width of the slices.

For the number of slices n_s, 6–8 are usually chosen. When the pole arc coefficient is consistent in the radial direction, the center of the radius R_m is taken as the calculation section to meet the accuracy requirements [25]. Thus, one slice is chosen in this article, and the average radius R_m is

$$R_m = \frac{R_o + R_i}{2} \tag{3}$$

where R_o and R_i are the outer and inner radius, respectively.

In this article, a 10-pole/12-slot AFPMM is introduced to validate the proposed nonlinear semi-AM. The parameters of AFPMM are given in Table I.

III. Harmonic Model Development

The model is formulated in the 2-D Cartesian coordinate system with the following assumptions.

1) In the 2-D model, the end effect of the motor is neglected.
2) The magnetic permeability in the stator slots and teeth is invariant in the radial direction and variant in the tangential direction.
3) Rotor backplates and stator yoke have infinite magnetic permeability.
4) The magnetic material has uniform magnetization, and the relative recoil permeability μ_{rec} is constant.
5) The current density has only one component along the y-axis.
6) Eddy-current effects are neglected.
7) The magnetic hysteresis phenomenon is neglected (i.e., only the initial magnetization curve was relied upon).

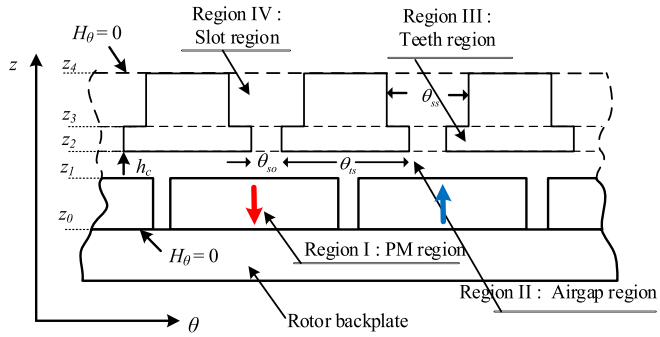

Fig. 2. Simplified model of AFPMM.

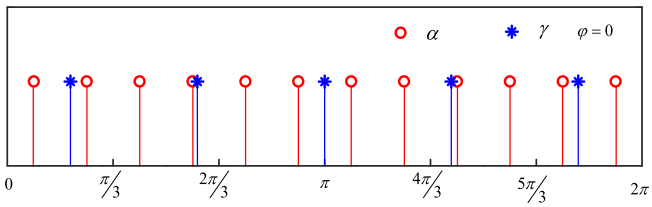

Fig. 3. Position of the *i*th stator slot opening and *k*th *N*-pole PM at $\varphi = 0$.

A. Investigation Model

The model is divided into simple types of regions, as shown in Fig. 2. Region I represents the PMs, region II is the air gap, region III is the stator teeth, and region IV is the stator slots.

Take a certain stator tooth center line as the initial position, the angular position of the *i*th stator slot opening and *k*th *N*-pole PM (see Fig. 3) is defined, respectively, by [23]

$$\alpha_i = \frac{2\pi}{Q_s} i - \frac{\pi}{Q_s} \tag{4}$$

$$\gamma_k = \frac{2\pi}{p/2}(k-1) + \varphi \tag{5}$$

where $1 \le i \le Q_s$, $1 \le k \le p/2$, and φ is the angle between a certain *N*-pole PM and the initial position.

B. Magnetic Field Derivation

According to Gauss's law of magnetism, the magnetic flux density vector B is divergence free, i.e., $\nabla \cdot B = 0$. In addition, according to Ampere's law of magnetism [26]

$$\nabla \times H = J. \tag{6}$$

The constitutive relation between B and H, given by

$$B = \mu_0 \mu_{rec} H + \mu_0 M \tag{7}$$

where M is the magnetization vector, μ_0 is the free space permeability, and μ_{rec} is the relative permeability of the PM.

Then, using the definition of A

$$B = \nabla \times A. \tag{8}$$

Poisson's equation is obtained by choosing Coulomb gauge

$$-\nabla^2 A = \mu_0 J + \mu_0 (\nabla \times M). \tag{9}$$

The magnetic field equation in Cartesian coordinates is

$$\frac{\partial^2 A}{\partial x^2} + \frac{\partial^2 A}{\partial z^2} = -\mu_0 \left(\frac{\partial M_z}{\partial x} - \frac{\partial M_x}{\partial z} \right) - \mu_0 J \tag{10}$$

where M_z and M_x are, respectively, the normal and tangential components of M, and J is the current density in the stator slots.

By using the following adaptation [27]:

$$x = \theta R_m. \tag{11}$$

Then, (10) can be rewritten as [16]

$$\frac{\partial^2 A}{\partial z^2} + \frac{1}{R_m^2} \frac{\partial^2 A}{\partial \theta^2} = -\mu_0 \left(\frac{1}{R_m} \frac{\partial M_z}{\partial \theta} - \frac{\partial M_x}{\partial z} \right) - \mu_0 J. \tag{12}$$

The matrix equation of fields $\boldsymbol{B_z}$ and $\boldsymbol{B_\theta}$ in the different regions is given by [22]

$$B_z = \frac{1}{R_m} \frac{\partial A}{\partial \theta} = -j \frac{1}{R_m} K_\theta A, \quad \text{and } B_\theta = -\frac{\partial A}{\partial z} \tag{13}$$

where $\boldsymbol{B_z}$ and $\boldsymbol{B_\theta}$ are the normal and tangential components of magnetic flux density, respectively, and K_θ is the diagonal matrix of harmonic order n, given by

$$K_\theta = \begin{bmatrix} -N & \cdots & 0 \\ \vdots & \ddots & \vdots \\ 0 & \cdots & N \end{bmatrix} \tag{14}$$

where N represents the highest spatial harmonic taken into account in the magnetic field solution.

Then, substituting (13) into (7), the expression for magnetic field strength in normal direction $\boldsymbol{H_z}$ and tangential direction $\boldsymbol{H_\theta}$ are obtained as

$$H_z = -j \frac{1}{R_m} \mu_{c,z}^{-1} K_\theta A, \text{ and } H_\theta = -\mu_{c,\theta}^{-1} \frac{\partial A}{\partial z} \tag{15}$$

where $\mu_{c,z}$, and $\mu_{c,\theta}$ are the normal and tangential relative permeability matrices, respectively.

Thus, $\nabla \times H = J$ can be rewritten in matrix form as

$$\frac{\partial H_\theta}{\partial z} + j \frac{1}{R_m} K_\theta H_z = J. \tag{16}$$

After substituting (15) into (16), the magnetic field equation for the inhomogeneous region is obtained as

$$\frac{\partial^2 A}{\partial z^2} - \frac{1}{R_m^2} V^2 A_z = -\mu_0 \frac{1}{R_m} M_\theta - j\mu_0 \frac{1}{R_m} S M_z - \mu_{c,\theta} J \tag{17}$$

where $V = (\mu_{c,\theta} K_\theta \mu_{c,z}^{-1} K_\theta)^{1/2}$ and $S = \mu_{c,\theta} K_\theta \mu_{c,z}^{-1}$.

Thus, A can be solved by using the separated variables method as

$$A = a_n e^{\frac{z}{R_m}} + b_n e^{-\frac{z}{R_m}} + R_m^2 F_1 + R_m F_2 \tag{18}$$

where

$$F_1 = -j\mu_0 V^{-2} \mu_{c,\theta} K_\theta \mu_{c,z}^{-1} M_z \tag{19}$$

$$F_2 = V^{-2} \mu_{c,\theta} J. \tag{20}$$

It has to be noted that the contribution of field sources is quite different from that in the polar coordinates system.

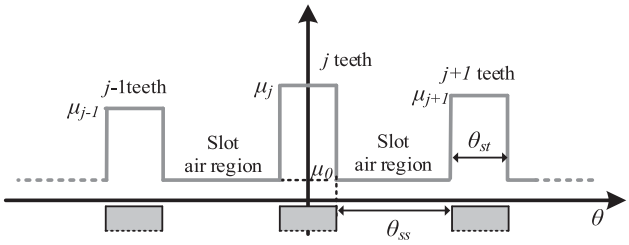

Fig. 4. Magnetic permeability distribution in region III.

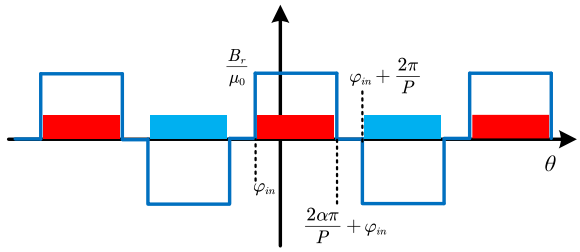

Fig. 5. Schematic of magnetization.

IV. Analytical Calculation

A. Permeability Convolution Matrix

Take region III as an example. The permeability distribution in region III is shown in Fig. 4 and is defined mathematically as [23]

$$\mu(\theta)=\begin{cases}\mu_0 & \theta\in\left[\alpha_i-\frac{\theta_{ss}}{2},\alpha_i+\frac{\theta_{ss}}{2}\right]\\ \mu_{\text{iron}} & \theta\in\left[\alpha_i-\frac{\theta_{ss}}{2}-\theta_{st},\alpha_i-\frac{\theta_{ss}}{2}\right]\end{cases}\tag{21}$$

where μ_{iron} is the permeability of ferromagnetic material in the stator teeth, which can be expressed as a truncated complex Fourier series, viz.,

$$\mu(\theta)=\sum_{n=-N}^{n=N}\hat{\mu}_n e^{-jn\theta}\tag{22}$$

where

$$\hat{\mu}_n=\begin{cases}\sum_{i=1}^{Q_s}\frac{1}{2\pi jn}\left[\mu_{\text{iron}}e^{-jn\frac{\theta_{ss}}{2}}\left(1-e^{-jn\theta_{st}}\right)\right.\\ \left.+2j\mu_0\sin\left(\frac{n\theta_{ss}}{2}\right)\right]e^{jn\alpha_i} & n\neq 0\\ \sum_{i=1}^{Q_s}\frac{1}{2\pi}\left(\mu_{\text{iron}}\theta_{st}+\mu_0\theta_{ss}\right) & n=0.\end{cases}\tag{23}$$

The normal and tangential relative magnetic permeability matrices $\mu_{c,z}$ and $\mu_{c,\theta}$ are defined by

$$\mu_{c,z}=\begin{bmatrix}\hat{\mu}_0 & \cdots & \hat{\mu}_{-2N}\\ \vdots & \ddots & \vdots\\ \hat{\mu}_{2N} & \cdots & \hat{\mu}_0\end{bmatrix},\quad \mu_{c,\theta}=\begin{bmatrix}\hat{\mu}_0^{rec} & \cdots & \hat{\mu}_{-2N}^{rec}\\ \vdots & \ddots & \vdots\\ \hat{\mu}_{2N}^{rec} & \cdots & \hat{\mu}_0^{rec}\end{bmatrix}^{-1}.\tag{24}$$

According to the fast Fourier series decomposition principle, (μ_0, μ_{iron}) can be replaced by ($1/\mu_0$, $1/\mu_{\text{iron}}$) to get $\hat{\mu}_n^{rec}$ [22].

B. Magnetization Source

It is assumed that magnetization is uniform throughout the PMs, as shown in Fig. 5.

In this article, the residual magnetization M is purely normal. Therefore, the tangential component $M_\theta=0$, and the normal component of M_z can be expressed as a truncated complex Fourier series [28], viz.,

$$M_z(\theta)=\sum_{n=-N}^{n=N}\hat{M}_{zn}e^{-jn\theta}\tag{25}$$

where

$$\hat{M}_{zn}=\frac{2pB_{\text{rem}}}{n\pi\mu_0}\sin\left(\frac{n\pi}{2p}\alpha_p\right).\tag{26}$$

where B_{rem} is the remanence flux density of PM.

C. Solution of the Poisson Equation

For the sake of clarity of the general solutions in different domains, the following notation is adopted in this article:

$$P_\omega(\alpha,\beta,\chi)=\alpha\left(e^{\frac{\beta-\chi}{\alpha}}\right)^\omega.\tag{27}$$

The general solution of (17) for each region is formulated by using the separation of variables method in z and θ, viz.,

$$A_I|_z=a_IP_{V_I}(R_m,z,z_1)+b_IP_{V_I}(R_m,z_0,z)+R_mF_1\tag{28}$$

$$A_{II}|_z=a_{II}P_{V_{II}}(R_m,z,z_2)+b_{II}P_{V_{II}}(R_m,z_1,z)\tag{29}$$

$$A_{III}|_z=a_{III}P_{V_{III}}(R_m,z,z_3)+b_{III}P_{V_{III}}(R_m,z_2,z)\tag{30}$$

$$A_{IV}|_z=a_{IV}P_{V_{IV}}(R_m,z,z_4)+b_{IV}P_{V_{IV}}(R_m,z_3,z)+R_m^2F_2.\tag{31}$$

On the premise of deriving the basic general solution, the magnetic field of each region can be obtained according to the boundary conditions.

Boundary conditions between two adjacent media are

$$A_I(z,\theta)=A_{II}(z,\theta)=0,H_\theta^I(z,\theta)=H_\theta^{II}(z,\theta)|_{z=z_1}\tag{32}$$

$$A_{II}(z,\theta)=A_{III}(z,\theta),H_\theta^{II}(z,\theta)=H_\theta^{III}(z,\theta)|_{z=z_2}\tag{33}$$

$$A_{III}(z,\theta)=A_{III}(z,\theta),H_\theta^{III}(z,\theta)=H_\theta^{IV}(z,\theta)|_{z=z_3}.\tag{34}$$

The Neumann boundary conditions are applied to the inner boundary of region I and the outer boundary of region IV

$$H_\theta^I|_{z=z_0}(z,\theta)=0,\ \text{and}\ H_\theta^{IV}|_{z=z_4}(z,\theta)=0.\tag{35}$$

According to the above boundary conditions, the magnetic vector potential A^k of each region can be obtained.

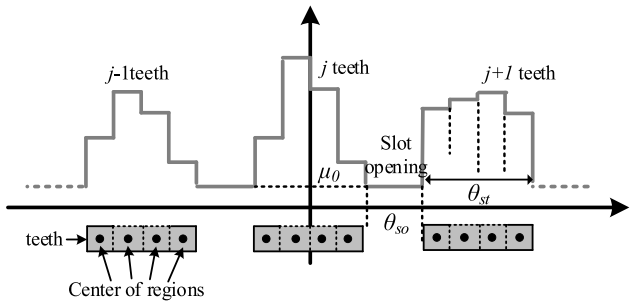

Fig. 6. Four calculation regions of stator teeth.

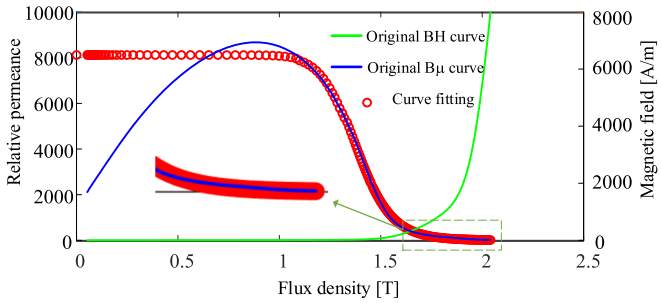

Fig. 7. Nonlinear modeling of ferromagnetic materials.

Then, the normal and tangential components of magnetic flux density B_z and B_θ of each region can be deduced from A^k

$$B_z^k|_z = -j\frac{1}{R_m}K_\theta A^k, \quad B_\theta^k|_z = -\frac{\partial A^k}{\partial z}. \tag{36}$$

D. Saturation Consideration

With regard to the PM machines, the tooth body is always designed at a nonsaturation region, while the teeth tip region would have high magnetic flux density. Therefore, the influence of stator tooth tip saturation is considered in this article. The stator tooth tip is divided into four calculation regions, as shown in Fig. 6 [24]. The maximum magnetic flux density point in each calculation region is used as the test point.

To consider the effect of local saturation of stator teeth in the saturated region, the permeability is calculated numerically by fitting the B–μ curve. The fitting equation is [29]

$$\mu_r(B) = \left(\frac{k_1}{\mu_0 k_2}\right)\left(\frac{1}{1+(B/k_1)^{k_3-1}}\right) \tag{37}$$

where k_1, k_2, and k_3 are the constants that depend on the iron type. In this article, the silicon steel sheet is 35CS300 (0.35 mm silicon steel sheets) and the laminated factor is 95%. The parameters k_1, k_2, and k_3 are 1.3844, 137.8334, and 17.4920, respectively.

Fig. 7 shows the original B–H curve and the comparison of the curve fitting waveform. It can be seen that this method has an error in the region when the magnetic flux density is small. However, in the unsaturated region, there is no significant difference between the results of $\mu_r = 8000$ and $\mu_r = 2000$. In the saturated region, $B > 1.7$ T, the curve agrees well with the original B–μ curve. Hence, the calculation accuracy is satisfied in this article.

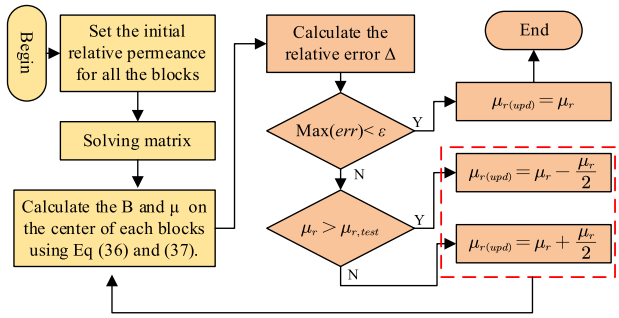

Fig. 8. Relative magnetic permeability update of stator teeth.

TABLE II
MESH INFORMATION OF FEM

Properties	3-D model	2-D slice model
Elements	692,452	19,543
Nodes	173,969	9,950
Minimum mesh size/mm	0.0336	0.251
Maximum mesh size/mm	0.998	0.998
Average mesh size/mm	0.646	0.762

Fig. 8 shows the iterative calculation flowchart of the stator tooth permeability. In the first step, the relative permeability of stator teeth is equal to the maximum value given by the curve fitting. The magnetic flux density of stator teeth B_t is obtained by the analytical calculation of the magnetic field, and the relative permeability μ_r is obtained according to the following equation:

$$\Delta_j^m = \frac{|\mu_{r,j}^m - \mu_{r,j,\text{test}}^m|}{\mu_{r,j,\text{test}}^m}. \tag{38}$$

The relative permeability error $\triangle_j^m$ of stator teeth is calculated, and the relative permeability of stator teeth is updated according to the error. When $\triangle_j^m$ meets the error requirement, the calculation is finished, where j represents the jth stator tooth, m represents the mth calculation area, and $1 \le j \le Q_s$, $1 \le m \le 4$.

V. VALIDATION

To verify the effectiveness of the proposed model, the AM results of air gap magnetic flux density components and electromagnetic performances are compared with those obtained by the FEM and experimental results.

A. Finite-Element Model

The studied AFPMM, in this article, is a single stator and a double rotor, and the FEM is established in commercial finite-element software JMAG. To simplify the calculation, a one-fourth model is established. Fig. 9(a) shows the no-load magnetic field distribution of the 3-D model, and Fig. 9(b)

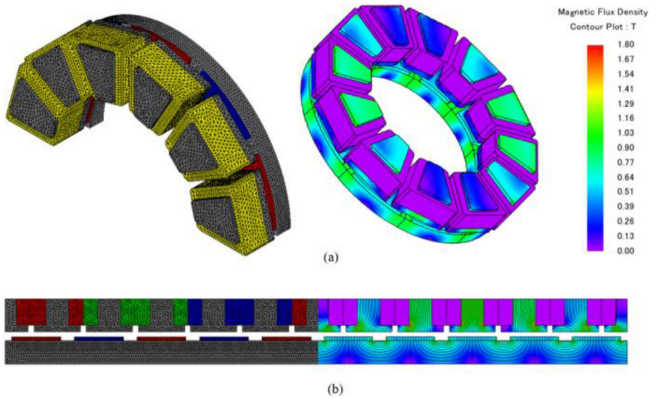

Fig. 9. FEM. (a) Three-dimensional model. (b) Two-dimensional slice model.

shows the no-load magnetic field and flux line distribution of the calculated section. The mesh information of the FEM is shown in Table II.

B. Comparison of Magnetic Field Distribution

The root-mean-square (RMS) error is used to evaluate the calculation accuracy of the AM proposed in this article [22]

$$\sigma = \sqrt{\frac{\sum_{i=1}^{N_{pc}} \left(\Omega_i^{\mathrm{FEA}} - \Omega_i^{\mathrm{HM}}\right)^2}{N_{pc}}} \tag{39}$$

where N_{pc} is the number of test data, and Ω can, respectively, stand for the magnetic flux density $\{B_z; B_\theta\}$, the back electromotive force (EMF), the cogging torque, and the output torque.

Fig. 10 shows the comparison of the normal and tangential components in the middle of the air gap between the FEM and the proposed AM. The RMS error of the normal and tangential components for the air gap magnetic flux density is 8 mT and 7 mT, respectively. It can be seen that very good agreement is achieved, which validates the high accuracy of the proposed model.

To verify the armature calculation, the PM sources are set as 0 T, the currents of coils are $i_a = 0$, $i_b = 5.196$ A, and $i_c = -5.196$ A. The magnetic field results from the armature are shown in Fig. 11. It can be seen that the results obtained by the proposed model match well with the FEM. The RMS error of the normal and tangential components for the air gap magnetic flux density is 11 mT and 9 mT, respectively.

It should be pointed out that the iron material is unsaturated in the previous study; to consider the local saturation further, the load condition is calculated, and the load current at a certain time is $i_a = 6$ A, $i_b = -3$ A, and $i_c = -3$ A. The magnetic flux densities and Fourier series of these components are shown in Figs. 12 and 13. Moreover, the traditional analytical calculation method is also compared.

From the comparison, it can be seen that the waveforms and harmonic values of the proposed model are close to those of the FEM. The saturation effect appears clearly in the results of the normal and tangential components of magnetic flux density. Taking the normal component as an example, the RMS error of

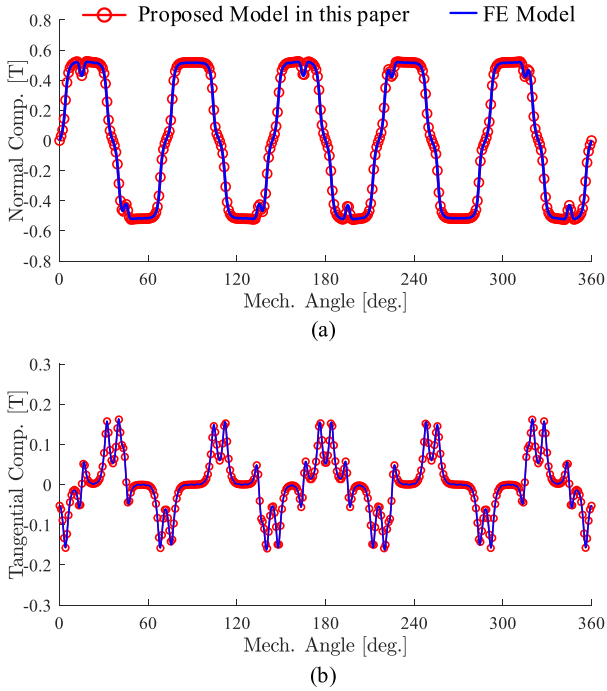

Fig. 10. Components of no-load magnetic flux density in the air gap (i.e., region II). (a) Normal. (b) Tangential.

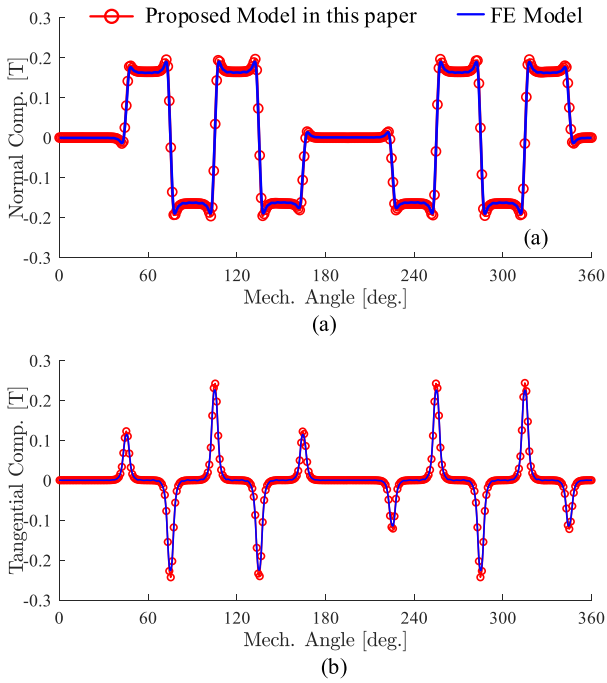

Fig. 11. Components of magnetic flux density caused by armature winding in the air gap (i.e., region II). (a) Normal. (b) Tangential.

the AM proposed in this article is 25 mT, while the traditional SD model is 31 mT. The magnetic saturation effect of ferromagnetic materials is taken into account in the model proposed in this article, so the RMS error is reduced by 19.4% compared with the traditional SD model (with $\mu \to +\infty$), and the calculation accuracy is improved.

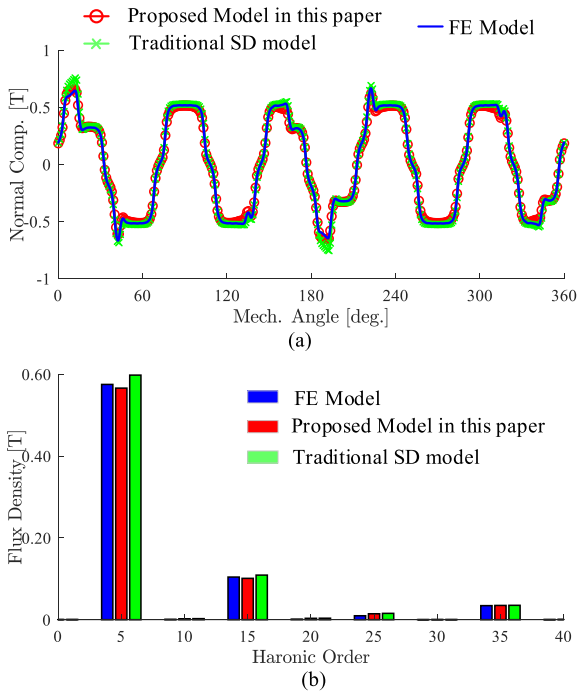

Fig. 12. Normal components of the on-load magnetic flux density in the air gap (i.e., region II). (a) Waveforms. (b) Harmonic spectrum.

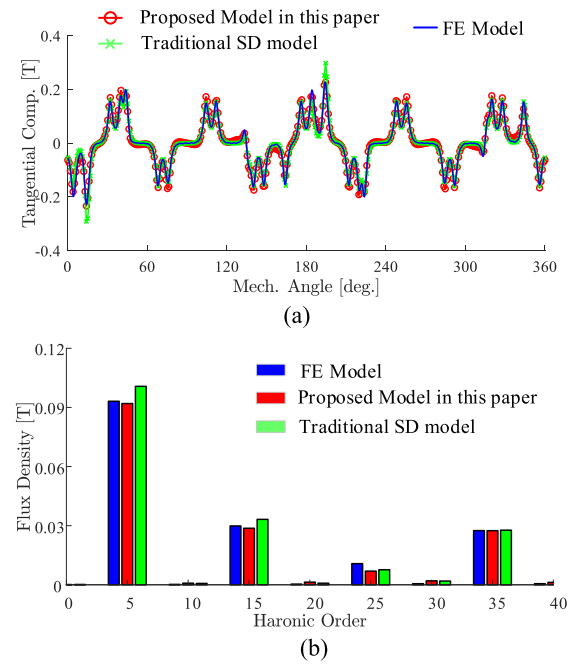

Fig. 13. Tangential components of the on-load magnetic flux density in the air gap (i.e., region II). (a) Waveforms. (b) Harmonic spectrum.

C. Spatial Harmonics Selection

To reduce the computational time of the nonlinear AM, the number of spatial harmonics N can be reduced. To assess the influence of N on the accuracy of the magnetic field calculation,

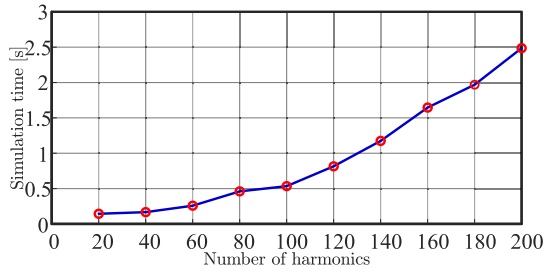

Fig. 14. Influence of the harmonics number on the calculation time.

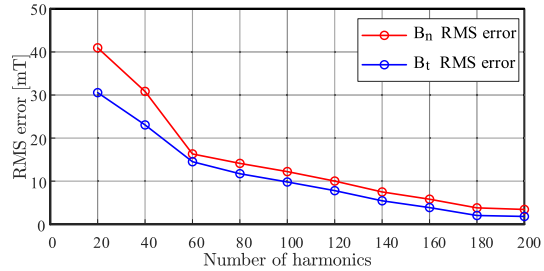

Fig. 15. Error for the normal and tangential components of the magnetic flux density in the air gap.

the RMS error between the results of nonlinear analytical calculations and the FEM is computed for various N, ranging from 20 to 200 in steps of 20.

In Fig. 14, the calculation time of the semi-AM is shown as a function of N. It can be seen that, for large N, the calculation time grows significantly with N. In Fig. 15, the error already starts to converge around $N = 140$, and the calculation time can be significantly decreased if a small increase in error is acceptable. Within the allowable range of error, selecting a reasonable harmonic number can speed up the solution and reduce the time in the initial design stage of the motor.

D. Iron Loss Computation

For the iron loss, the calculation of iron core loss is defined by the basic Steinmetz method. The iron core is expressed as [28]

$$P_{\text{iron}} = k_h f^{\alpha} B^{\beta} + k_e f^2 B^2 \tag{40}$$

where k_h, k_e, α, and β are, respectively, the coefficient of hysteresis loss, excess loss, and constants of steel material. For the material 35CS300, by using the curve fitting technique, the coefficients are calculated as 0.009, 0.0001, 1.171, and 2, respectively. f is the frequency and B is the iron core magnetic flux density.

In the no-load conditions, the normal and tangential magnetic flux density waveforms in the stator tooth of the proposed method [see Fig. 16(a) and (b)] have a similar shape to that of FEM. In Fig. 16(c) and (d), the iron loss evolutions in the stator teeth according to rotor speed under different current excitations are illustrated, respectively. As expected, in the side part of stator teeth, the iron losses have relatively large errors (10% under 8 A). This may be caused by the large magnetic fluctuations, and this

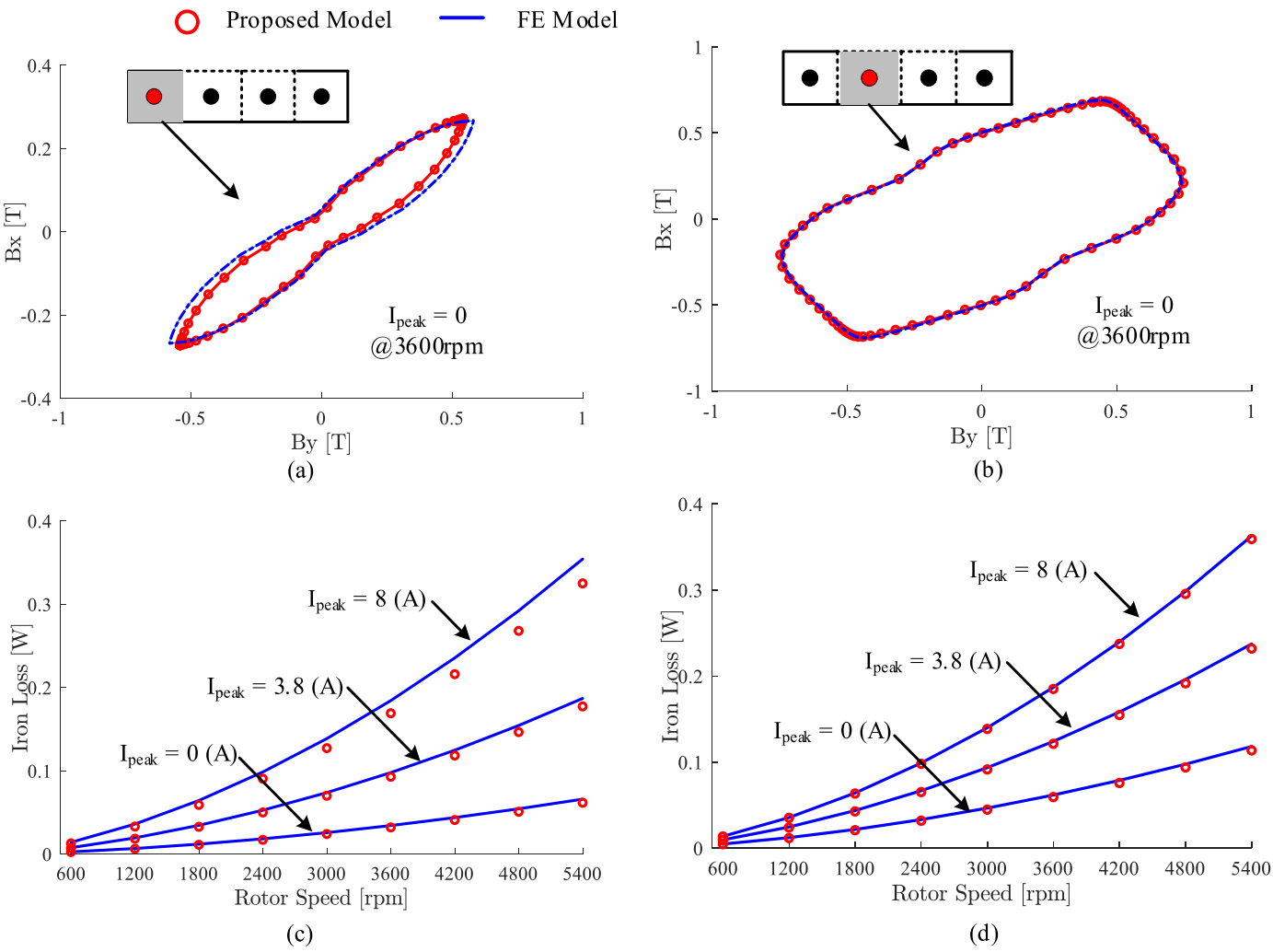

Fig. 16. Loci of the magnetic flux density at no load for a point on the (a) side of teeth, (b) middle of teeth; the iron loss evolution of (c) side of teeth, (d) middle of teeth.

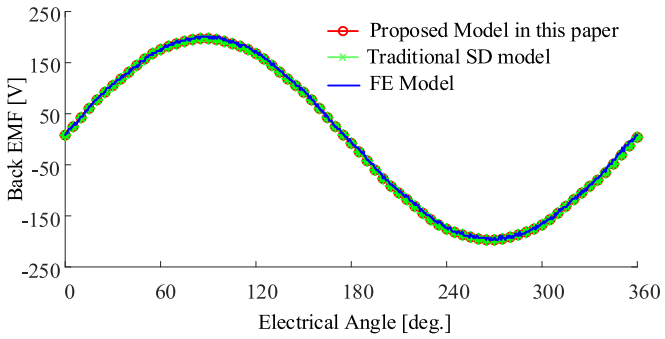

Fig. 17. Back EMF of phase *A* at 3600 r/min.

can be reduced by dividing the stator teeth into a large number. In the second part of stator teeth, we can observe that the iron losses are matched well. The comparison between the proposed model and FEM shows good agreement in both no-load and on-load conditions.

E. Comparison of Magnetic Performance

The phase back EMF can be calculated by magnetic theory; take phase *A* as an example [25]

$$E_a = N_c \frac{d\psi_a}{dt} \tag{41}$$

where N_c is the number of coil turns, and Ψ_a is the magnetic flux linkage defined by

$$\psi_a = l_{stk} \frac{N_c}{S} \sum_{i=1}^{Q_s} \int_{\alpha_i + \frac{\theta_{ss}}{2} - d}^{\alpha_i + \frac{\theta_{ss}}{2}} \int_{z_3}^{z_4} A_z^{IV}(z,\theta)\, dz d\theta. \tag{42}$$

In this article, the output torque of the motor is calculated by the Maxwell stress tensor method, the intermediate position of the air gap is selected as the integral path, and the output torque can be calculated by [25]

$$T = \frac{t_{cp} R_{calc}^2}{\mu_0} \int_0^{2\pi} B_n B_\theta \, d\theta. \tag{43}$$

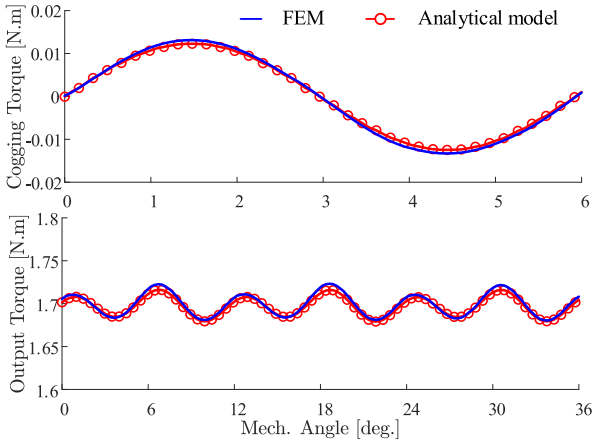

Fig. 18. Cogging and output (viz., electromagnetic) torque waveform.

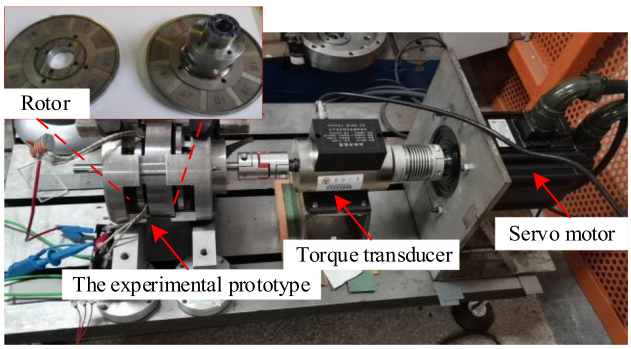

Fig. 19. Test platform of AFPMM.

In the no-load condition, the ferromagnetic material has no obvious saturation phenomenon, so the back EMF waveform obtained by the traditional SDM is in good agreement with the results obtained by the nonlinear AM and the FEM, as shown in Fig. 17. The RMS errors of the traditional SDM and the nonlinear AM are 1.68% and 0.83%, respectively. Fig. 18 shows the results of the electromagnetic and cogging torque, which are in good agreement with those obtained from the FEM model.

F. Experimental Validation

According to the AFPMM parameters, as given in Table I, an experimental prototype is manufactured to verify the correctness of the proposed nonlinear AM. The AFPMM experimental platform is shown in Fig. 19.

The back EMF, cogging torque, and output torque of the prototype were measured. The experimental results were compared with the AM.

The line back EMFs of the AFPMM prototype were tested at 1000 r/min. Fig. 20 shows the comparison of line back EMF between the AM and experimental results of the back EMF. It can be seen from the figure that the nonlinear semi-AM agrees well with the experimental result, and the RMS error is only 0.57 V. The experimental results show that the AM proposed

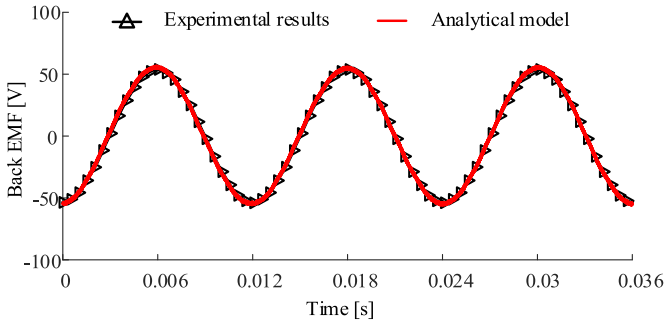

Fig. 20. Comparison of the line back EMFs between analytical results and experimental results at 1000 r/min.

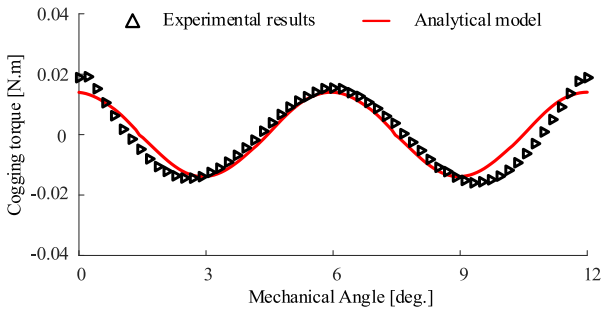

Fig. 21. Cogging torque between AM and experimental results.

TABLE III
CURRENT AND TORQUE DATA AT 3600 R/MIN

Current RMS/A	2.21	2.498	2.759	3.028	3.652
Test/Nm	1.4	1.589	1.763	1.94	2.34
FEM/Nm	1.46	1.65	1.82	2.0	2.40
AM/Nm	1.465	1.654	1.81	1.99	2.38

in this article has high accuracy and meets the requirements of engineering calculation.

The cogging torque of the prototype was measured by the leverage measurement method. The experimental results are shown in Fig. 21. The results show that the numerical value is in good agreement with the waveform and conforms to the law of change. Due to the small cogging torque fluctuation, assembly precision, and bearing friction of the prototype, the error of the maximum deviation point between analytical results and test data is up to 30%.

As for the electromagnetic torque of the proposed model and experiment, we tested the output torque at 1800 r/min and 3600 r/min, respectively, and the current versus torque curve is shown in Fig. 22. Table III lists the detailed data of the current RMS and output torque at 3600 r/min.

In Table III, the maximum error between the proposed model and experimental results is less than 5%, i.e., when the current is 135.3% of the rated current, the relative error is 1.73%. The difference between the predicted and the experimental results is due to the experimental errors and the assumptions presented in

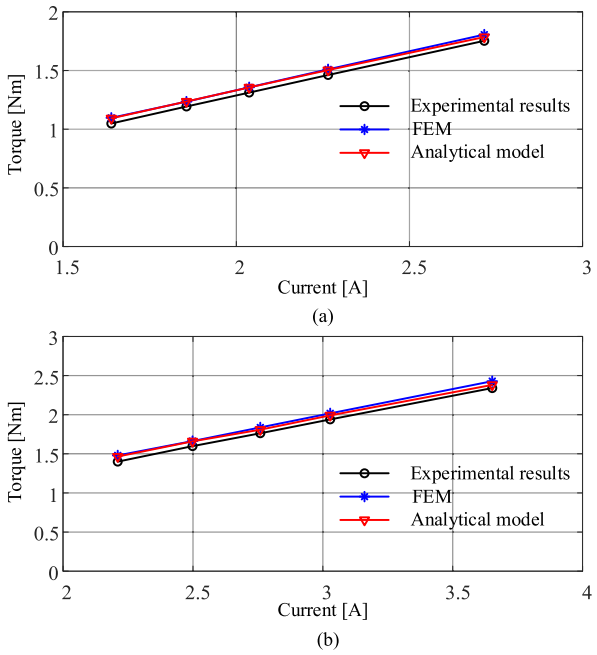

Fig. 22. Output (i.e., electromagnetic) torque. (a) 1800 r/min. (b) 3600 r/min.

Section III, the most important of which is the neglect of eddy-current effects and magnetic hysteresis phenomenon. Overall, the error is within reasonable limits.

VI. Conclusion

In this article, we presented the first reported HM technique in Cartesian coordinates. The calculation equations and strategy were given in this article; the results showed that the proposed model can consider the local magnetic saturation and have high accuracy for calculating both the magnetic flux density and the electromagnetic performances. More accurate predictions may be obtained by dividing the iron part into more small pieces with reasonable harmonic orders.

Moreover, the proposed model in this article was not limited to AFPMMs, and it can also be applied to other types of machines, for instance, the flat PM linear machines. This will be done in the following research.

Appendix

The following notation is adopted:

$$P(\lambda,\alpha,\beta,\chi)=\left(\frac{e^{\frac{\beta}{\alpha}}}{e^{\frac{\chi}{\alpha}}}\right)^{\lambda} \tag{44}$$

$$P_a^I = P(V_I, R_m, z, z_1) \tag{45}$$

$$P_b^I = P(V_I, R_m, z_0, z) \tag{46}$$

$$P_a^{II} = P(V_{II}, R_m, z, z_2) \tag{47}$$

$$P_b^{II} = P(V_{II}, R_m, z_1, z) \tag{48}$$

$$P_a^{III} = P(V_{III}, R_m, z, z_3) \tag{49}$$

$$P_b^{III} = P(V_{III}, R_m, z_2, z) \tag{50}$$

$$P_a^{IV} = P(V_{IV}, R_m, z, z_4) \tag{51}$$

$$P_b^{IV} = P(V_{IV}, R_m, z_3, z) \tag{52}$$

$${B_n}^I|_z = -K_\theta \left[P_a^I a_I + P_b^I b_I - j\mu_0 V^{-2}\mu_{c,\theta}^I K_\theta \left(\mu_{c,z}^I\right)^{-1} M_{z1}\right] \tag{53}$$

$$B_\theta^I|_z = -V_I\left[P_a^I a_I - P_b^I b_I\right] \tag{54}$$

$$B_n^{II}|_z = -K_\theta\left[P_a^{II} a_{II} + P_b^{II} b_{II}\right] \tag{55}$$

$$B_\theta^{II}|_z = -V_{II}\left[P_a^{II} a_{II} - P_b^{II} b_{II}\right] \tag{56}$$

$$B_n^{III}|_z = -K_\theta\left[P_a^{III} a_{III} + P_b^{III} b_{III}\right] \tag{57}$$

$$B_\theta^{III}|_z = -V_{III}\left[P_a^{III} a_{III} - P_b^{III} b_{III}\right] \tag{58}$$

$$B_n^{IV}|_z = -K_\theta\left[P_a^{IV} a_{IV} + P_b^{IV} b_{IV} + R_m V_{IV}^{-1}\mu_{c,\theta}^{IV} J_z\right] \tag{59}$$

$$B_\theta^{IV}|_z = -V_{IV}\left[P_a^{IV} a_{IV} - P_b^{IV} b_{IV}\right] \tag{60}$$

$$H_n^{I,II,III,IV} = \left[\mu_{c,z}^{I,II,III,IV}\right]^{-1} B_n^{I,II,III,IV} \tag{61}$$

$$H_\theta^{I,II,III,IV} = \left[\mu_{c,\theta}^{I,II,III,IV}\right]^{-1} B_\theta^{I,II,III,IV}. \tag{62}$$

Representing all the matrix equations obtained by interface condition in matrix-form yields

$$\begin{bmatrix} a_I \\ b_I \\ a_{II} \\ b_{II} \\ a_{III} \\ b_{III} \\ a_{IV} \\ b_{IV} \end{bmatrix} = \begin{bmatrix} M_{11} & M_{12} & 0 & 0 & 0 & 0 & 0 & 0 \\ M_{21} & M_{22} & M_{23} & M_{24} & 0 & 0 & 0 & 0 \\ M_{31} & M_{32} & M_{33} & M_{34} & 0 & 0 & 0 & 0 \\ 0 & 0 & M_{43} & M_{44} & M_{45} & M_{46} & 0 & 0 \\ 0 & 0 & M_{53} & M_{54} & M_{55} & M_{56} & 0 & 0 \\ 0 & 0 & 0 & 0 & M_{65} & M_{66} & M_{67} & M_{68} \\ 0 & 0 & 0 & 0 & M_{75} & M_{76} & M_{77} & M_{78} \\ 0 & 0 & 0 & 0 & 0 & 0 & M_{87} & M_{88} \end{bmatrix}^{-1} \cdot \begin{bmatrix} 0 \\ Y_1 \\ 0 \\ 0 \\ 0 \\ Y_2 \\ 0 \\ 0 \end{bmatrix} \tag{63}$$

$$P(\lambda,\alpha,\beta,\chi)=\left(\frac{e^{\frac{\beta}{\alpha}}}{e^{\frac{\chi}{\alpha}}}\right)^{\lambda} \tag{64}$$

$$P_I = P(V_I, R_m, z_0, z_1) \tag{65}$$

$$P_{II} = P(V_{II}, R_m, z_1, z_2) \tag{66}$$

$$P_{III} = P(V_{III}, R_m, z_2, z_3) \tag{67}$$

$$P_{IV} = P\left(V_{IV}, R_m, z_3, z_4\right). \tag{68}$$

The entries of the matrix form of the submatrices are represented as follows:

$$M_{11} = P_I \tag{69}$$
$$M_{12} = -I \tag{70}$$
$$M_{21} = I \tag{71}$$
$$M_{22} = P_I \tag{72}$$
$$M_{23} = -P_{II} \tag{73}$$
$$M_{24} = -I \tag{74}$$
$$M_{31} = \left(\mu_{c,\theta}^{I}\right)^{-1} \cdot V_I \tag{75}$$
$$M_{34} = \left(\mu_{c,\theta}^{II}\right)^{-1} \cdot V_{II} \tag{76}$$
$$M_{32} = -\left(\mu_{c,\theta}^{I}\right)^{-1} \cdot V_I \cdot P_I \tag{77}$$
$$M_{33} = -\left(\mu_{c,\theta}^{II}\right)^{-1} \cdot V_{II} \cdot P_{II} \tag{78}$$
$$M_{34} = \left(\mu_{c,\theta}^{II}\right)^{-1} \cdot V_{II} \tag{79}$$
$$M_{43} = I \tag{80}$$
$$M_{44} = P_{II} \tag{81}$$
$$M_{45} = -P_{III} \tag{82}$$
$$M_{46} = -I \tag{83}$$
$$M_{53} = \left(\mu_{c,\theta}^{II}\right)^{-1} \cdot V_{II} \tag{84}$$
$$M_{54} = -\left(\mu_{c,\theta}^{II}\right)^{-1} \cdot V_{II} \cdot P_{II} \tag{85}$$
$$M_{55} = -\left(\mu_{c,\theta}^{III}\right)^{-1} \cdot V_{III} \cdot P_{III} \tag{86}$$
$$M_{56} = \left(\mu_{c,\theta}^{III}\right)^{-1} \cdot V_{III} \tag{87}$$
$$M_{65} = I \tag{88}$$
$$M_{66} = P_{III} \tag{89}$$
$$M_{67} = -P_{IV} \tag{90}$$
$$M_{68} = -I \tag{91}$$
$$M_{75} = \left(\mu_{c,\theta}^{III}\right)^{-1} \cdot V_{III} \tag{92}$$
$$M_{76} = -\left(\mu_{c,\theta}^{III}\right)^{-1} \cdot V_{III} \cdot P_{III} \tag{93}$$
$$M_{77} = -\left(\mu_{c,\theta}^{IV}\right)^{-1} \cdot V_{IV} \cdot P_{IV} \tag{94}$$
$$M_{78} = \left(\mu_{c,\theta}^{IV}\right)^{-1} \cdot V_{IV} \tag{95}$$
$$M_{87} = I \tag{96}$$
$$M_{88} = -P_{IV} \tag{97}$$
$$Y_1 = -j\mu_0 V_I^{-2} \mu_{c,\theta}^{I} K_\theta \left(\mu_{c,z}^{I}\right)^{-1} M_z \tag{98}$$
$$Y_2 = R_m V_{IV}^{-2} \mu_{c,\theta}^{IV} J_z. \tag{99}$$

REFERENCES

[1] N. J. Stannard, J. G. Washington, and G. J. Atkinson, "A comparison of axial field topologies employing SMC for traction applications," in *Proc. 19th Int. Conf. Elect. Mach. Syst.*, Nov. 2016, pp. 1–6.

[2] N. M. Hung, D. M. Cuong, D. N. Hung, and D. H. Du, "Design axial flux permanent magnet machine for in-wheel of electric vehicle," in *Proc. Adv. Eng. Res. Appl.*, Cham, Switzerland, 2020, pp. 220–228, doi: 10.1007/978-3-030-37497-6_26.

[3] J. F. Gieras, R.-J. Wang, and M. J. Kamper, *Axial Flux Permanent Magnet Brushless Machines*. New York, NY, USA: Springer, 2008.

[4] M. U. Lampérth, A. C. Malloy, A. Mlot, and M. Cordner, "Assessment of axial flux motor technology for hybrid powertrain integration," *World Electr. Veh. J.*, vol. 7, no. 2, pp. 187–194, Jun. 2015, doi: 10.3390/wevj7020187.

[5] M. Thiele, "Analysis of cogging torque due to manufacturing variations in fractional pitch permanent magnet synchronous machines," M.S. thesis, School Eng. Inf. Technol., Charles Darwin Univ., Casuarina, NT, Australia, Nov. 2013.

[6] R. Benlamine, F. Dubas, S.-A. Randi, D. Lhotellier, and C. Espanet, "3-D numerical hybrid method for PM eddy-current losses calculation: Application to axial-flux PMSMs," *IEEE Trans. Magn.*, vol. 51, no. 7, Jul. 2015, Art. no. 8106110, doi: 10.1109/TMAG.2015.2405053.

[7] A. Hemeida *et al.*, "A simple and efficient quasi-3D magnetic equivalent circuit for surface axial flux permanent magnet synchronous machines," *IEEE Trans. Ind. Electron.*, vol. 66, no. 11, pp. 8318–8333, Nov. 2019, doi: 10.1109/TIE.2018.2884212.

[8] K. J. W. Pluk, J. W. Jansen, and E. A. Lomonova, "Hybrid analytical modeling: Fourier modeling combined with mesh-based magnetic equivalent circuits," *IEEE Trans. Magn.*, vol. 51, no. 8, Aug. 2015, Art. no. 8106812, doi: 10.1109/TMAG.2015.2419197.

[9] R. Benlamine, F. Dubas, S.-A. Randi, D. Lhotellier, and C. Espanet, "Modeling of an axial-flux interior PMs machine for an automotive application using magnetic equivalent circuit," in *Proc. 18th Int. Conf. Elect. Mach. Syst.*, Oct. 2015, pp. 1266–1271, doi: 10.1109/ICEMS.2015.7385234.

[10] H. W. Derbas, J. M. Williams, A. C. Koenig, and S. D. Pekarek, "A comparison of nodal- and mesh-based magnetic equivalent circuit models," *IEEE Trans. Energy Convers.*, vol. 24, no. 2, pp. 388–396, Jun. 2009, doi: 10.1109/TEC.2008.2002037.

[11] T. A. Driscoll and L. N. Trefethen, *Schwarz-Christoffel Mapping*. Cambridge, U.K.: Cambridge Univ. Press, 2002.

[12] L. J. Wu, Z. Li, X. Huang, Y. Zhong, Y. Fang, and Z. Q. Zhu, "A hybrid field model for open-circuit field prediction in surface-mounted PM machines considering saturation," *IEEE Trans. Magn.*, vol. 54, no. 6, Jun. 2018, Art. no. 8103812, doi: 10.1109/TMAG.2018.2817178.

[13] A. Alipour and M. Moallem, "Analytical magnetic field analysis of axial flux permanent-magnet machines using Schwarz-Christoffel transformation," in *Proc. Int. Electr. Mach. Drives Conf.*, May 2013, pp. 670–677, doi: 10.1109/IEMDC.2013.6556166.

[14] E. Ilhan, E. T. Motoasca, J. J. H. Paulides, and E. A. Lomonova, "Conformal mapping: Schwarz-Christoffel method for flux-switching PM machines," *Math. Sci.*, vol. 6, no. 1, pp. 1–9, Sep. 2012, doi: 10.1186/2251-7456-6-37.

[15] T. Lubin, S. Mezani, and A. Rezzoug, "Exact analytical method for magnetic field computation in the air gap of cylindrical electrical machines considering slotting effects," *IEEE Trans. Magn.*, vol. 46, no. 4, pp. 1092–1099, Apr. 2010, doi: 10.1109/TMAG.2009.2036257.

[16] T. Lubin, S. Mezani, and A. Rezzoug, "Simple analytical expressions for the force and torque of axial magnetic couplings," *IEEE Trans. Energy Convers.*, vol. 27, no. 2, pp. 536–546, Jun. 2012, doi: 10.1109/TEC.2012.2183372.

[17] F. Dubas and K. Boughrara, "New scientific contribution on the 2-D subdomain technique in Cartesian coordinates: Taking into account of iron parts," *Math. Comput. Appl.*, vol. 22, no. 1, pp. 1–39, Feb. 2017, doi: 10.3390/mca22010017.

[18] L. Roubache, K. Boughrara, F. Dubas, and R. Ibtiouen, "New subdomain technique for electromagnetic performances calculation in radial-flux electrical machines considering finite soft-magnetic material permeability," *IEEE Trans. Magn.*, vol. 54, no. 4, Apr. 2018, Art. no. 8103315, doi: 10.1109/TMAG.2017.2785254.

[19] B. Ladghem-Chikouche, K. Boughrara, F. Dubas, and R. Ibtiouen, "2-D semi-analytical magnetic field calculation for flat permanent-magnet linear machines using exact subdomain technique," *IEEE Trans. Magn.*, vol. 57, no. 6, Jun. 2021, Art. no. 8106211, doi: 10.1109/TMAG.2021.3068326.

[20] L. Roubache, K. Boughrara, F. Dubas, and R. Ibtiouen, "Elementary subdomain technique for magnetic field calculation in rotating electrical machines with local saturation effect," *COMPEL, Int. J. Comput. Math. Electr. Electron. Eng.*, vol. 28, no. 1, pp. 24–45, Jan. 2018, doi: 10.1108/COMPEL-11-2017-0481.

[21] R. L. J. Sprangers, J. J. H. Paulides, B. L. J. Gysen, J. Waarma, and E. A. Lomonova, "Semianalytical framework for synchronous reluctance motor analysis including finite soft-magnetic material permeability," *IEEE Trans. Magn.*, vol. 51, no. 11, Nov. 2015, Art. no. 8110504, doi: 10.1109/TMAG.2015.2442419.

[22] R. L. J. Sprangers, J. J. H. Paulides, B. L. J. Gysen, and E. A. Lomonova, "Magnetic saturation in semi-analytical harmonic modeling for electric machine analysis," *IEEE Trans. Magn.*, vol. 52, no. 2, Feb. 2016, Art. no. 8100410, doi: 10.1109/TMAG.2015.2480708.

[23] Z. Djelloul-Khedda, K. Boughrara, F. Dubas, and R. Ibtiouen, "Nonlinear analytical prediction of magnetic field and electromagnetic performances in switched reluctance machines," *IEEE Trans. Magn.*, vol. 53, no. 7, Jul. 2017, Art. no. 8107311, doi: 10.1109/TMAG.2017.2679686.

[24] H. Zhao, C. Liu, Z. Song, and J. Yu, "A fast optimization scheme of coaxial magnetic gears based on exact analytical model considering magnetic saturation," *IEEE Trans. Ind. Appl.*, vol. 57, no. 1, pp. 437–447, Jan./Feb. 2021, doi: 10.1109/TIA.2020.3040142.

[25] B. Guo, Y. Huang, F. Peng, J. Dong, and Y. Li, "Analytical modeling of misalignment in axial flux permanent magnet machine," *IEEE Trans. Ind. Electron.*, vol. 67, no. 6, pp. 4433–4443, Jun. 2020, doi: 10.1109/TIE.2019.2924607.

[26] M. Hajdinjak and D. Miljavec, "Analytical calculation of the magnetic field distribution in slotless brushless machines with U-shaped interior permanent magnets," *IEEE Trans. Ind. Electron.*, vol. 67, no. 8, pp. 6721–6731, Aug. 2020, doi: 10.1109/TIE.2019.2939967.

[27] T. Lubin, S. Mezani, and A. Rezzoug, "Development of a 2-D analytical model for the electromagnetic computation of axial-field magnetic gears," *IEEE Trans. Magn.*, vol. 49, no. 11, pp. 5507–5521, Nov. 2013, doi: 10.1109/TMAG.2013.2267746.

[28] Z. Djelloul-Khedda, K. Boughrara, F. Dubas, A. Kechroud, and A. Tikellaline, "Analytical prediction of iron-core losses in flux-modulated permanent-magnet synchronous machines," *IEEE Trans. Magn.*, vol. 55, no. 1, Jan. 2019, Art. no. 6300112, doi: 10.1109/TMAG.2018.2877164.

[29] A. Hemeida and P. Sergeant, "Analytical modeling of surface PMSM using a combined solution of Maxwell–s equations and magnetic equivalent circuit," *IEEE Trans. Magn.*, vol. 50, no. 12, Dec. 2014, Art. no. 7027913, doi: 10.1109/TMAG.2014.2330801.

Baocheng Guo (Member, IEEE) received the B.E. degree in electrical engineering from the China University of Petroleum, Qingdao, China, in 2009, the M.E. degree in electrical engineering from the Harbin University of Science and Technology, Harbin, China, in 2014, and the Ph.D. degree in electrical engineering from Southeast University, Nanjing, China, in 2017.

He has been an Assistant Professor with Nanjing Normal University (NNU), Nanjing, China, since 2020. Before joining NNU, he was a Postdoctoral Researcher with Southeast University. His main interests are the electromagnetic field computation and development of fast multiphysics models of electrical machines.

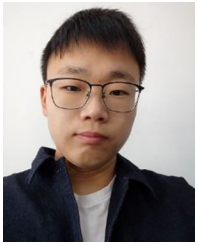

Yunlu Du received the B.S. degree in electrical engineering from Anhui University, Hefei, China, in 2020. He is currently working toward the Ph.D. degree in electrical engineering with the School of Electrical Engineering, Southeast University, Nanjing, China.

His main research interests include the electromagnetic field computation and permanent magnet motor design.

Zakarya Djelloul-Khedda was born in Chlef, Algeria, in 1988. He received the B.Sc. degrees from the Hassiba Benbouali University of Chlef, Ouled Fares, Algeria, in 2009, the M.Sc. degrees from the Hassiba Benbouali University of Chlef, Ouled Fares, Algeria, and the Ph.D. degree from the Djilali Bounaama University of Khemis Miliana, Khemis Miliana, Algeria, in 2011 and 2019, respectively, both in electrical engineering .

He is currently with SADEG Company, Sonelgaz Group, Algiers, Algeria, which is an Algerian national group of companies responsible for the production, transmission, and distribution of electricity and natural gas. His current research interests include design, modeling, optimization, and control of electrical machines.

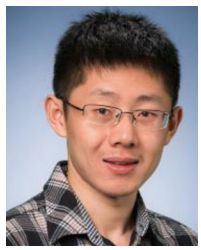

Fei Peng (Member, IEEE) received the B.S. and M.S. degrees in electrical engineering from Southeast University, Nanjing, China, in 2010 and 2012, respectively, and the Ph.D. degree in electrical and computer engineering from McMaster University, Hamilton, ON, Canada, in 2016.

After that, he was a Postdoctoral Fellow with the McMaster Institute for Automotive Research and Technology, McMaster University. In December 2016, he joined the School of Electrical Engineering, Southeast University, as an Assistant Professor. His research interests include optimal design and control of power converters, modeling, and digital control of motor drives.

Jianning Dong (Member, IEEE) received the B.S. and Ph.D. degrees in electrical engineering from Southeast University, Nanjing, China, in 2010 and 2015, respectively.

Since 2016, he has been an Assistant Professor with DC System, Energy Conversion and Storage Group, Delft University of Technology (TU Delft), Delft, The Netherlands. Before joining TU Delft, he was a Postdoctoral Researcher with McMaster Automotive Resource Centre, McMaster University, Hamilton, ON, Canada. His research interests include electromechanical energy conversion and contactless power transfer.

Yunkai Huang received the M.Sc. and Ph.D. degrees in electrical engineering from Southeast University, Nanjing, China, in 2001 and 2007, respectively.

He is currently a Professor with the School of Electrical Engineering, Southeast University, and teaching Electrical Machinery and Digital Signal Processing. His research interests include design and control of PM machine and high-speed machine, applications in domestic appliances, electric vehicles, railway traction, all electric ships, and wind power generation systems.

Frédéric Dubas was born in Vesoul, France, in 1978. He received the M.Sc. and Ph.D. degrees in electrical engineering from University Bourgogne Franche-Comté, Besançon, France, in 2002 and 2006, respectively, with a focus on the design and the optimization of high-speed surface-mounted permanent-magnet (PM) synchronous motor for the drive of a fuel cell air-compressor.

From 2014 to 2016, he was the Head of Unconventional Thermal and Electrical Machines Team. He is the Head of Electrical Actuators Group, Hybrid & Fuel Cell Systems, Electrical Machines Team. He works with Alstom Transports, Ornans, France, and Renault Technocenter, Guyancourt, France, where he is involved in the modeling, design, and optimization of electrical systems and, in particular, induction and PM synchronous (radial and/or axial flux) machines, creative problem solving, and electrical propulsion/traction. He is currently an Associate Professor with the Department of Energy, FEMTO-ST Institute, Belfort, France, and University Bourgogne Franche-Comté, Besançon, France. He has authored more than 100 refereed publications and holds a patent about the manufacturing of axial-flux PM machines with flux focusing. His research interests include applied mathematics, partial differential equations, separation of variables method, principle of superposition, (semi-)analytical modeling, subdomain technique, magnetic equivalent circuit, and electrical machines.

Dr. Dubas was the recipient of the Prize Paper Award, IEEE VPPC, in 2005, Prize Presentation Award, WASET ICEMS, in 2017, RENAULT Internal Award, Direction Engineering Alliance—Innovation, in 2019, and Best Paper Award, IEEE ICEMS, in 2021.

Kamel Boughrara was born in Algiers, Algeria, in 1969. He received the Engineer Diploma degree from Ecole Nationale Polytechnique (ENP), Algiers, Algeria, in 1994, the Magister degree from the University of Sciences and Technology Houari Boumediene, Algiers, Algeria, and the Ph.D. degree from ENP, Algiers, Algeria, in 1997 and 2008, respectively, both in electrical engineering.

He is currently a Professor with ENP, where he is also the Head of the Department of Electrical Engineering. His current research interest includes the modeling and control of electrical machines.